PERGAMON

International Journal of Heat and Mass Transfer 41 (1998) 3961–3978

International Journal of HEAT and MASS TRANSFER

Conjugate heat transfer of a finned oval tube with a punched longitudinal vortex generator in form of a delta winglet—parametric investigations of the winglet

Y. Chen, M. Fiebig, N. K. Mitra*

Ruhr-Universität Bochum, Institut für Thermo- und Fluiddynamik, 44780 Bochum, Germany

Received 12 September 1997; in final form 6 February 1998

Abstract

To explore the influences of the angle of attack and the aspect ratio of a winglet, which is punched near the leading edge of the fin in a high performance finned oval tube (FOT), on the heat transfer enhancement (HTE) and flow loss penalty (FLP), three-dimensional flow and conjugate heat transfer in a FOT were calculated for a thermally and hydrodynamically developing laminar flow ($Re = 300$) by solving the Navier–Stokes and energy equations with a Finite-Volume Method in body-fitted grids. The conjugate heat transfer was realized by iterations of the energy equation in the flow field and of the conduction equation in the fin. Three angles of attack ($\beta = 20^\circ$, 30° and 45°) and two aspect ratios ($\Lambda = 1.5$ and 2) were investigated. Velocity and temperature fields, vortex formation, local heat transfer distributions and global results are presented. The winglet with $\beta = 30^\circ$ and $\Lambda = 2$ provides the best ratio of HTE to FLP with $(j/j_0)/(f/f_0) = 1.04$.

Nomenclature

a thermal diffusivity, coefficient
A area
b span
B width
h convective heat transfer coefficient; height of the winglet
H channel height
J Jacobian
k thermal conductivity
L length
p pressure
R_P thermohydraulic performance factor
t time
T temperature
u, v, w velocity components
x, y, z Cartesian co-ordinates
α central angle
β cofactor, angle of attack
Λ aspect ratio
ξ, η, ζ generalized co-ordinates
δ fin thickness
ν kinematic viscosity
ρ density
ϕ general variable.

Subscripts and superscripts

0 reference value
B bulk
cs cross section
f fin
frt frontal
ht heat transfer
i, j, k index
m mean value
sp span averaged
T tube
VG vortex generator
w wall, winglet
z_0 $z = 0$ or $z = 1$
* dimensional (as superscript).

Dimensionless parameters and variables

$Bi = h^*\delta^*/k_f^*$ Biot number

* Corresponding author. Tel.: 00 49 234 700 6444; fax: 00 49 234 709 4162.

0017–9310/98 $19.00
PII: S0017–9310(98)00076–3

$$f_{app} = \frac{\Delta P^*}{\rho^* u_0^{*2}/2} \frac{A_{frt}^*}{A_{ht}^*}$$ friction factor

$$Fi = \frac{k_f^*}{k^*} \frac{\delta^*}{H^*}$$ fin parameter 1

$$Ft = \frac{a_f^*}{a^*} \frac{1}{Pe}$$ fin parameter 2

$$j = \frac{Nu_m}{Re\, Pr^{1/3}}$$ Colburn j factor

$$Nu = \frac{h^* H^*}{k^*} = \frac{\dot{q}_{z0}}{(T_f - T_B)}$$ Nusselt number

$Pe = Re\, Pr$ Peclet number

$Pr = v^*/a^*$ Prandtl number

$$\dot{q} = \left.\frac{\partial T}{\partial z}\right|_{z=0} - \left.\frac{\partial T}{\partial z}\right|_{z=1}$$ heat flux on the fin

$$Re = \frac{u_0^* H^*}{v^*}$$ Reynolds number.

Abbreviations

DW delta wing
DWP delta winglet pair
FLP flow loss penalty
FOT finned oval tube
HTE heat transfer enhancement
LVs longitudinal vortices
LVG longitudinal vortex generators
RW rectangular wing
RWP rectangular winglet pair
SIMPLEC semi-implicit method for pressure linked equations, consistent
SIP strong implicit procedure
VG vortex generator
WVG wing-type vortex generator.

1. Introduction

Fins as used in a finned tube heat exchanger (see Fig. 1) are secondary surfaces which reduce the thermal resistance by enlarging the transfer surface on the gas side where heat transfer is normally very poor due to the thermophysical properties of gases. The difference of the heat transfer coefficients on the gas and liquid side can be so large, that a very large area ratio of fin to tube (up to two orders of magnitude) is needed to balance the resistance on both sides. But the effectiveness and thus the economy of fins decreases quickly with increasing area ratio. Heat transfer enhancement (HTE) on fins is therefore necessary. Mechanisms for passive HTE are: (1) developing boundary layers; (2) swirl; and (3) flow destabilization.

The wing-type vortex generators (WVG), which have recently been intensively investigated [1–6], can generate

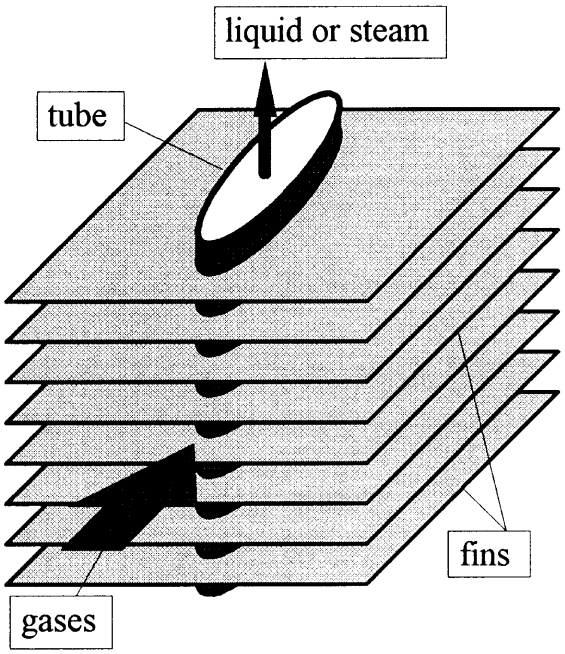

Fig. 1. Part of a finned flat-tube heat exhanger core.

all three mechanisms for passive HTE. Four basic WVG forms—delta wing (DW), rectangular wing (RW), delta winglet pair (DWP) and rectangular winglet pair (RWP) can be punched, embossed or mounted on the heat transfer surface with an angle of attack β (see Fig. 2(a), 2(b)). The aspect ratio of a VG is defined as $\Lambda = b^2/A_{VG}$, where b is the span and A_{VG} the surface area of the VG. Flow separation from the edges of the VG generates vortices. Vortices with their rotation axes normal to the main flow direction are called transverse vortices (TVs), and those with their axes aligned with the main flow are called longitudinal vortices (LVs). VGs with $\beta < 65^\circ$ generate mainly LV and are called longitudinal VG (LVG) [7]. Figure 2(c) depicts the main LVs generated by RWPs.

The optimum geometric parameters of the winglets depend on the geometry of the flow passage and the flow structure. For plate heat exchangers Tiggelbeck [7] and Güntermann [8] investigated experimentally and numerically the influence of the geometry on the performance of winglets. For the best ratio of HTE to flow loss penalty (FLP) of a DWP ($\Lambda = 2, h = H$), β is 45° for a developing flow in a duct with $Re = 2300$ [7], while it is 15° for a very compact arrangement of rectangular winglet pairs (RWP) ($\Lambda = 0.5$, $h = H/2$) in a periodically fully developed flow with $Re = 1000$ [8]. A VG with $\Lambda = 1.5$ generates maximum HTE, while a VG with $\Lambda = 2$ produces the best ratio of HTE to FLP [7]. The distance from the leading edge of the fin to the tip of the winglet was also varied. The difference in Nusselt numbers

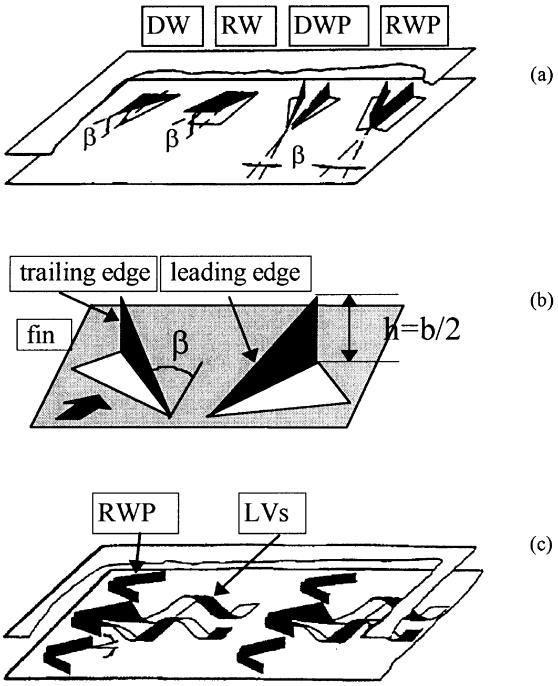

Fig. 2. Schematic of vortex generators and their vortices. (a) Four basic WVG forms; (b) a punched-up DWP; (c) RWP-array and LVs.

remains within the experimental accuracy for the distances of H, $2H$ and $3H$ [7].

A finned tube element differs from a plate heat exchanger element with isothermal plate in: (a) different flow structure and boundary conditions due to the no-slip conditions on the tube wall and its blockage to the passage; (b) different temperature distribution in the flow passage due to the heat transfer to the tube (heat source or sink); and (c) nonisothermal fin temperature due to the conjugate heat transfer in a finned tube element [9, 10]. For a finned circular tube with a punched DWP ($\beta = 45^\circ$, $\Lambda = 1.5$, $h = H$), numerical investigations [11–13] show that the DWP delays the flow separation from the tube, deflects the flow to the tube wake, drags fluid from the recirculation zone to the main flow, intensifies mixing by swirling the flow and thus enhances the heat transfer. It can also avoid local heat transfer reversal on the fin in the tube wake [11, 13]. For a finned flat tube with embossed and punched staggered rows of RWP in a developing flow with Re in the range of 500 and 2000, experimental investigations [14] show that LVGs with $\beta = 20$–30° and $h = 0.5H$ are the most promising, and a ratio of Colburn 'j' to 'f' factor of more than 0.5 is achieved. Experimental investigation [15] shows that HTE by mounted DWP ($\beta = 45^\circ$, $\Lambda = 2$, $h = H$) in finned flat tubes is more pronounced than in a finned circular tube, and the DWPs should be located in the upstream side of the tube with a distance of two tube widths between the tips of the winglets.

For a tube-fin element with a flat tube a numerical investigation of heat transfer enhancement by vortex generators has never been reported. The experiments [15] have been carried out with mounted DWPs whereas punched DWPs are relevant in practice. Furthermore, the influences of the number of DWPs, of their geometry, e.g. Λ, β, and of their location with respect to the tube have never been investigated. Here lies the scope of the present paper.

The purposes of this paper are: (1) to investigate in detail the formation of the swirling flow by punched DWPs in a finned oval tube; and (2) to study the influences of β, Λ and location of a DWP on HTE and FLP, aiming to optimize a single winglet as a background knowledge for further performance improvement with more winglets.

2. Theoretical formulation and solution procedure

2.1. *Geometrical model*

Figure 3(a) shows an FOT element with a punched DWP. Two fins with thickness d form a channel of height H, width B ($= 9.1H$) and length L ($= 15.4H$). An oval tube ($L_T/B_T = 5.5$, cross sectional area $A_{T,CS} = 24.6H^2$) is located at the center of the fin. The ratio of fin to tube area is 8.44. Such a geometry is commonly used in industry [16]. A DWP is punched out of each fin near the entrance. The thickness of the winglet is assumed to be zero and the height of the DWP (h) is equal to the channel height (H) so that the DWP can also function as a pitch holder of the fin. In the y-direction, the mid-points of the winglets are located at $y = 1.68H$, which corresponds to the middle of the free flow passage in y-direction.

Heat transfer distribution of an FOT without DWP [10] shows that in the Reynolds number range of 100–500, the leading edge effect of the fin ceases at $x \approx H$, preceding the influence of the tube. To investigate the influence of a slightly changed location of the winglet in the streamwise direction on the performance of the winglet, two winglet locations were investigated. In the first location the tip of the winglet was at $x_{PA} = 1.46$. The second location was in the middle of the leading edge of the fin ($x = 0$) and the front stagnation point of the tube ($x = 1.26$), i.e. $x_{PA} = 0.63$. The better x-position of them was selected for further investigations with β, which was varied to 20°, 30° and 45°. The best β was then selected for a computation with $\Lambda = 1.5$. Table 1 lists the parameter and location of the winglets in the investigated configurations.

For small Reynolds numbers, the flow is steady and the computational domain can be reduced by using symmetry conditions on the mid-plane of the channel

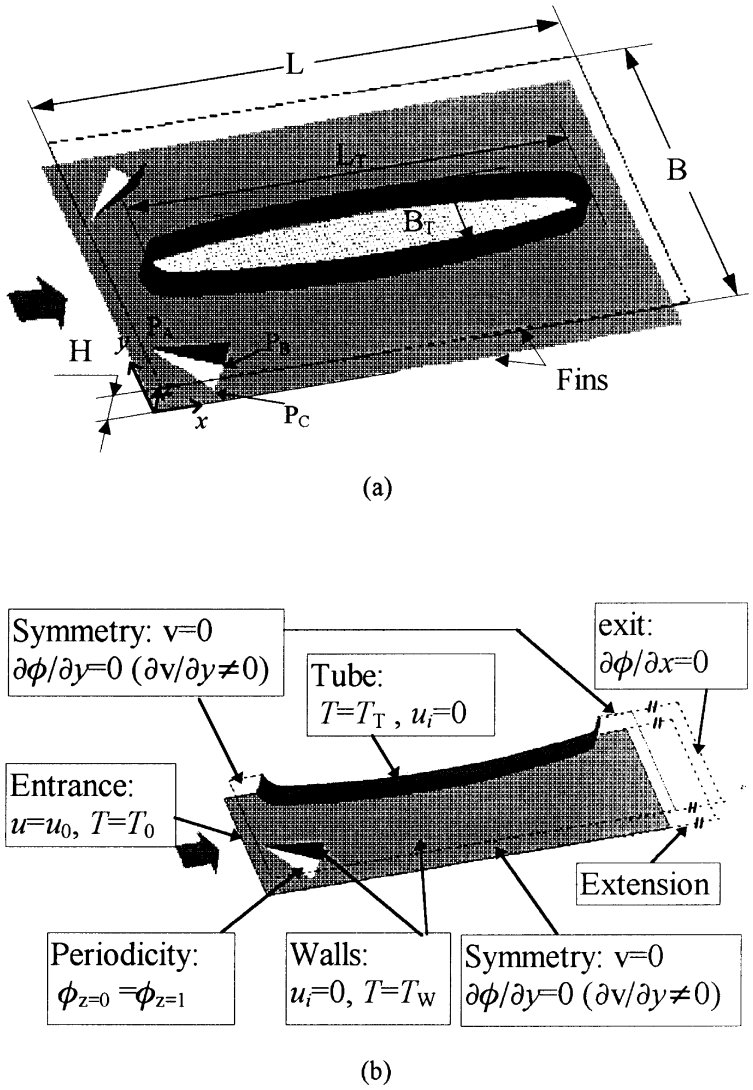

Fig. 3. (a) The geometrical model ($L = 15.4H$, $B = 9.1H$, $L_T = 12.8H$, $B_T = 2.4H$, $A_f/A_T = 8.44$); (b) the computational domain with boundary conditions.

Table 1
The winglet position of the investigated configurations

config.	β	Λ	x_{PA}	y_{PA}	x_{PB}	y_{PB}	x_{PC}	y_{PC}
1	45°	2	1.46	2.41	2.87	1.00	2.16	0.29
2	45°	2	0.63	2.41	2.04	1.00	1.33	0.29
3	30°	2	0.63	2.19	2.36	1.19	1.86	0.32
4	20°	2	0.63	2.03	2.51	1.35	2.17	0.41
5	30°	1.5	0.63	2.36	2.93	1.03	2.43	0.16

The area ratio of DWP to fin is 1.73% for configs. 1–4 and 2.3% for config. 5. The points P_A, P_B, and P_C are defined in Fig. 3(a).

($y = B/2$). Figure 3(b) shows the computational domain and the boundary conditions. To employ the gradient boundary conditions, the domain is extended by $6H$ over the exit to ensure a recirculation-free flow there. No-slip velocity boundary conditions were used on solid walls (tube and fin).

2.2. Mathematical model

The velocity and temperature fields in the channel were calculated by solving the unsteady three dimensional Navier-Stokes and energy equations for an incompressible fluid with constant properties ($Pr = 0.7$). The

temperature field in the fin was obtained by solving the conduction equation. In dimensionless form these equations in curvilinear coordinate system with Cartesian velocity components and in index notation are,

$$\frac{\partial U_i}{\partial \xi_i} = 0 \tag{1}$$

$$J\frac{\partial u_k}{\partial t} + \frac{\partial}{\partial \xi_i}\left[U_i u_k - \frac{1}{Re}\frac{1}{J}\left(B^i_j \frac{\partial u_k}{\partial \xi_j} + \beta^i_j \omega^j_k\right) + p\beta^i_k\right] = 0 \tag{2}$$

$$J\frac{\partial T}{\partial t} + \frac{\partial}{\partial \xi_i}\left[U_i T - \frac{1}{Pe}\frac{1}{J}\left(B^i_j \frac{\partial T}{\partial \xi_j}\right)\right] = 0 \tag{3}$$

$$\frac{1}{Ft}J\frac{\partial T_f}{\partial t} - \frac{\partial}{\partial \xi_i}\left[\frac{1}{J}\left(B^i_j \frac{\partial T_f}{\partial \xi_j}\right)\right] = \frac{1}{Fi}J\dot{q} \tag{4}$$

with

$$U_i = u_j\beta^i_j, \quad B^i_j = \beta^i_k\beta^j_k, \quad \omega^i_j = \frac{\partial u_i}{\partial \xi_k}\beta^k_j$$

and

$$Re = \frac{u^*_0 H^*}{\nu^*}, \quad Pr = \frac{\nu^*}{a^*}, \quad Pe = Re\,Pr,$$

$$Fi = \frac{\delta^*}{H^*}\frac{k^*_f}{k^*}, \quad Ft = \frac{1}{Pe}\frac{a^*_f}{a^*}$$

where Einstein summation convention applies and dissipation is neglected. β^i_j are the cofactors of $\partial x_i/\partial \xi_j$ in the Jacobian J of the coordinate transformation $x_i = x_i(\xi_j)$. Re, Pr, and Pe are the Reynolds number, the Prandtl number and the Peclet number respectively. Assuming very small Biot number on the fin, the conduction in the fin becomes two-dimensional. The conjugate heat transfer is described by two parameters Fi and Ft. Their significance has been explained in [9, 11].

In the eqns (1)–(4), the time is nondimensionalized by H^*/u^*_0, all lengths by H^*, the velocity components by the average velocity u^*_0. The temperature is the difference between the local and the inlet temperature scaled by the difference of the tube temperature and the inlet temperature. The pressure is the difference between the local and a reference pressure divided by $\rho^* u^{*2}_0$. Variables with a subscript '0' refer to the state of the fluid at the entrance, with an 'f' to the fin, and with a 'T' to the tube. The dimensionless temperatures at the inlet T_0 and on the tube T_T are 0 and 1 respectively. In eqn (4), $\dot{q}$ stands for the convective heat removal on both sides of the fin. This term couples the convective heat transfer to the fins and conductive heat transfer in the fins. It can be expressed as:

$$\dot{q} = \dot{q}|_{z=0} - \dot{q}|_{z=1} \quad \text{with}$$

$$\dot{q}|_z = \frac{1}{J}\left(\frac{\partial T}{\partial \xi}\beta^1_3 + \frac{\partial T}{\partial \eta}\beta^2_3 + \frac{\partial T}{\partial \zeta}\beta^3_3\right)_z \tag{5}$$

where $\dot{q}|_{z=0}$ and $\dot{q}|_{z=1}$ denote the heat removal on the lower and upper side of the fin. They are nondimensionalized by dividing

$$\frac{(T^*_T - T^*_0)k^*}{H^*}.$$

2.3. Numerical solution

A grid generation technique by solving the Poisson equation [17] was used to discretize the computational domain into a finite number of control volumes. The winglet with zero thickness was approximated by the interface between two control volumes. The differential equations (1)–(4) were discretized by a finite-volume method [18]. The convective terms were discretized with a 'flux blending' scheme, in which the convective flux was split into an upwind difference (UD) and a central difference (CD), and was treated with a 'deferred-correction approach' [19], in which the UD part was calculated implicitly, while the difference between the CD and UD part was calculated explicitly. SIMPLEC algorithm [20] were used for pressure-velocity correction. To avoid decoupling of the velocity and pressure field caused by the co-located arrangement of the dependent variables, a momentum interpolation was applied [21]. The algebraic equation system was solved by the strongly implicit procedure (SIP) of Stone [22], in which the original coefficient matrix was incompletely split into a product of a lower and a upper matrix and solved iteratively. More descriptions of the solution procedure can be found in [23–25]. The numerical solution of the velocity and temperature fields for one time step was carried out with the following procedure:

(1) The momentum equations were solved with the best available initial values;
(2) A pressure-velocity correction based on SIMPLEC was performed;
(3) Steps 1 and 2 were repeated until a divergence-free velocity field was obtained.
(4) The energy equation was solved with the known velocity field and the best available temperature field on the fin and in the fluid;
(5) The local heat fluxes to the fin $\dot{q}(x,y)$ were calculated;
(6) The heat conduction equation was solved with the local heat flux as heat sources.

Steps (4) to (6) were repeated until a converged solution is obtained.

2.4. Validation of the procedure

The basic program code was used to compute complex oscillating flow in ducts with vortex generator [26] and flows in hydrodynamic couplings [24, 27]. Some validation studies have been reported there. The code and the basis configuration used in this study were the same

as those in the investigation of the flow and heat transfer in an FOT without DWP [10]. Computations were performed on an IBM-RISC-System/6000/530H on body-fitted grids of 187*52*25 (configs. 1–2), 152*60*24 (configs. 3, 5) and 152*52*25 (config. 4) points along x, y and z coordinates. A divergence-free criterion of 10^{-5} was prescribed. For an FOT with $Re = 300$ and $Fi = 500$, the grid convergence index by Roache [28] is 1.338% for the apparent friction number f and 3.51% for the Colburn j factor [25].

Figure 4 compares the computed and reference [29] Nusselt number distributions in a developing duct flow with constant wall temperature. Both curves have an inflection point around $x = 1$, where the largest deviation of the numerical result from the reference curve appears. The reference curve has a smoother profile in that region. The mean Nusselt number of the numerical result is about 3.2% smaller than that of the reference value. The computed apparent friction factor f_{app} is about 3% higher than that calculated with the correlation formula for hydrodynamically developing duct flow as recommended by Shah and Bhatti [29].

Figure 5 compares the measured spanwise averaged Nusselt number distribution, based on the fluid temperature at the entrance, with the computed Nu in the FOT with constant fin temperature. In the experiment the Nusselt numbers were deduced from the heat and mass transfer analogy and the ammonia absorption measurements (AAM) performed on an FOT model in a windtunnel at Reynolds number 1090 [30]. Beginning at $x = 4$ the measured and the computed results agree perfectly. But there are 11.5%, 9.8% and 5.0% dis-

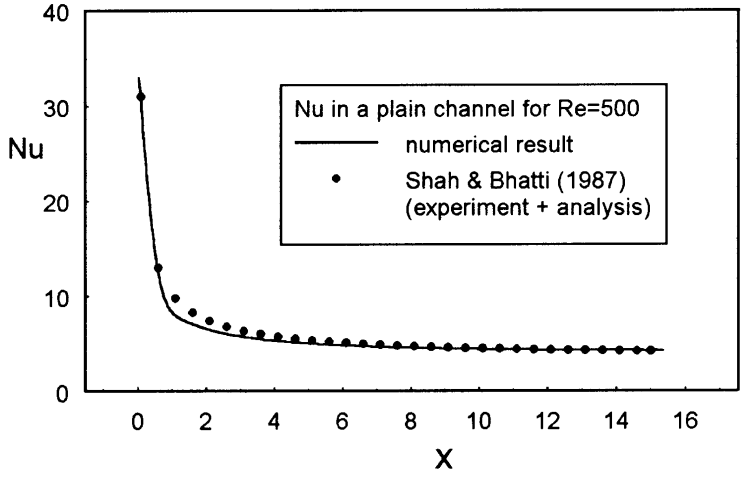

Fig. 4. Analytical–numerical comparison of the Nusselt number distribution in a plain channel of simultaneous developing flow for $Re = 500$.

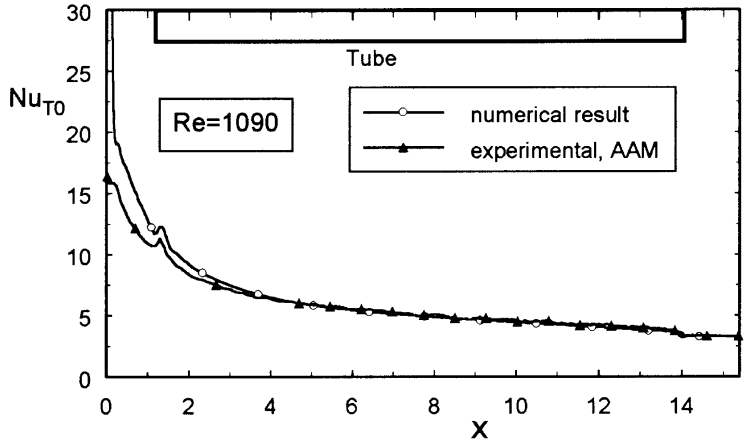

Fig. 5. Experimental–numerical comparison of the Nusselt number distribution in an FOT with constant fin temperature for $Re = 1090$.

crepancy at $x = 1$, 2, and 3 respectively. The reason for this discrepancy may be the difference of the velocity distribution at the entrance. For the computation, a uniform velocity distribution was employed at the entrance. For the experiment, great effort was made to realize a homogeneous velocity at the inlet. However the influence of the wall and the blockage at the leading edge of the test section cannot be avoided. Besides, an exact measurement of the mass transfer at the leading edge by ammonia absorption technique is nearly impossible [31, 32]. In Fig. 4, the agreement of the numerical and the reference results near the entrance is much better than that in Fig. 5. Comparing Figs 4 and 5, we find that the numerical results lie between the reference and the experimental results.

3. Flow patterns, temperature field and local heat transfer

3.1. *Flow patterns*

In order to study the generation and structure of primary and secondary vortices, we plotted the streamlines starting from different grid points of the leading edge and the trailing edge of the VG. Figure 6 shows the streamlines from the winglet leading edge for config. 1 at $Re = 300$. Here $\Delta z = 0$ stands for the line on the leading edge; positive or negative values of Δz indicate parallel lines above or below the winglet leading edge. Figure 6(a) shows the streamlines starting from the points covering 1/4 length (beginning at the tip) of the winglet leading edge at $\Delta z = -0.025$. These streamlines braid together to form the core of the primary vortex, see the secondary velocity vectors on the exit plane in Fig. 6(a). Figure 6(b) and 6(c) shows the streamlines from the half and the full length of the leading edge. These form the streamlines in and around the core. Figure 6(d)–6(f) show streamlines from different heights over the full length of the leading edge. The fluid over the leading edge with a distance up to $\Delta z = 0.175$ constitutes the body of the LVs (see Fig. 6(d)–(f)). In this height, the streamlines weave like a shell of a snail. The rotational velocity decreases with Δz, while the diameter of the shell increases with Δz. For $\Delta z \geqslant 0.225$, (sec Fig. 6(g)–(i)), the rotation of the fluid becomes weaker. The streamlines from this region compose the transition layer surrounding the LVs. Figure 7 shows the streamlines starting at the trailing edge of the winglet. Here $\Delta y = 0$ represents the trailing edge and negative Δy indicates away from the trailing edge. The streamlines participating in the primary LVs decrease with increasing distance to the trailing edge. The fluid immediately behind the trailing edge takes part in the primary LVs, with exception of the two streamlines from the lowest corner (see Fig. 7(a)). For $\Delta y = -0.05$, about 75% of the streamlines in the upper part joins the primary LVs (see Fig. 7(b)). The remaining 25% in the lower part do not join the primary LVs, but flow in the surrounding of the primary LVs. Some of them join the induced vortices, which result from the interaction of the primary vortex with the wall [33]. For $\Delta y = -0.15$, -0.25 and -0.35, about 60%, 50% and 25% of the streamlines near the upper channel wall join the primary LVs respectively (see Fig. 7(c)–(e)). Beginning with $\Delta y = -0.045$, the flow is hardly influenced by the winglet (see Fig. 7(f)).

The angle of attack of a winglet influences the strength and the form of the vortices. Figure 8 compares the secondary velocity vectors and their streamlines in eight x-sections for config 2, 3 and 4 ($\beta = 45^\circ$, 30°, 20°) with $Re = 300$. In this range of β, the magnitude of the secondary velocity vectors decreases with decreasing β, and the difference of the magnitude between $\beta = 30^\circ$ and 20° is larger than that between $\beta = 45^\circ$ and 30° (see Fig. 8(a)–(c)). In Fig. 8(d)–(f), the ratio of the width to height of the LVs changes from section to section and depends on β. From near the winglet to far downstream, the shape of the vortices generated by the winglet with $\beta = 45^\circ$ changes from flat to circular, while that by the winglet with $\beta = 20^\circ$ from circular to flat. The shape of the vortices generated by the winglet with $\beta = 30^\circ$ shows less change in their shape and keeps nearly in circular form in all sections (see Fig. 8(e)). If the winglets are projected to a plane normal to the streamwise direction (here the y–z-plane), the ratios of the projected width to height of the winglets are 1.41, 1.00 and 0.68 for $\beta = 45^\circ$, 30° and 20° respectively. The shape of the vortices seems not to be determined by these ratios, as is also demonstrated by the vortices generated by a delta winglet with $\beta = 30^\circ$ and $\Lambda = 1.5$ (the ratios of the projected width to height of the winglet is 1.33), (see Fig. 9). The streamlines in the vortex cross sections for $\Lambda = 1.5$ seem to be rounder than those for $\Lambda = 2$. The magnitude of the secondary flow generated by the winglet with $\Lambda = 1.5$ is much larger than that with $\Lambda = 2$. The difference of the magnitude of the secondary velocities decreases with increasing streamwise distance from the winglet.

The pressure difference between the stagnation and the suction side of the winglet forces the fluid from the leading edge to the suction side and to form vortices. From the outer surface of the LVs to the LV-core, the pressure decreases gradually as shown in Fig. 10. The minimum pressure lines, where the core of the longitudinal vortices is located, does not occur at the geometrical middle of the winglet, but shifts to the side of the trailing edge. The pressure difference between the wake and its surrounding is larger for $\beta = 45^\circ$ than for $\beta = 30^\circ$.

3.2. *Temperature field and local heat transfer*

Qualitatively the temperature distributions on the fin with and without winglets are similar (see [10]), except

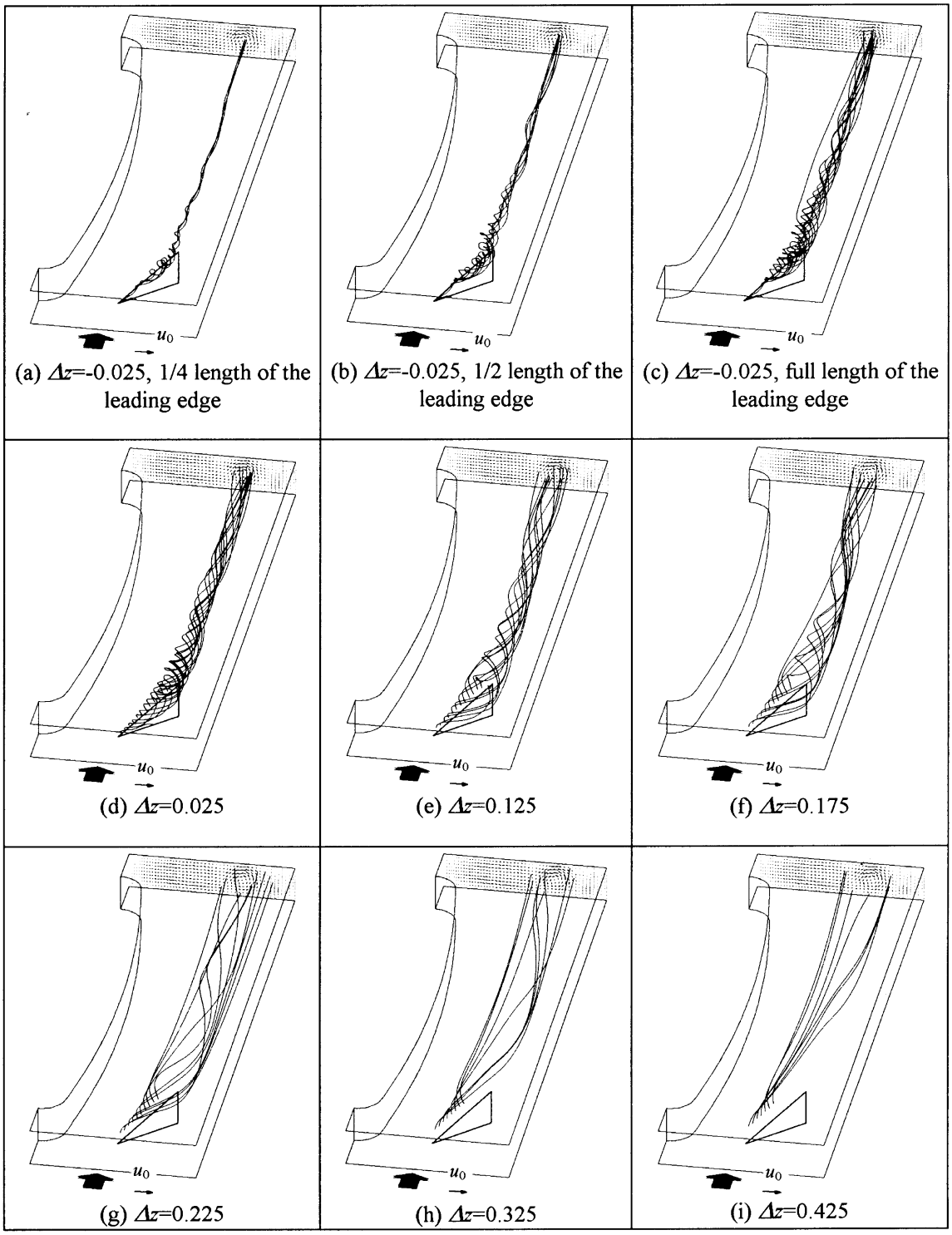

Fig. 6. Streamlines starting from different distances over the leading edge of the winglet, config. 1, $Re = 300$. $\Delta z = 0$ stands for the line on the leading edge.

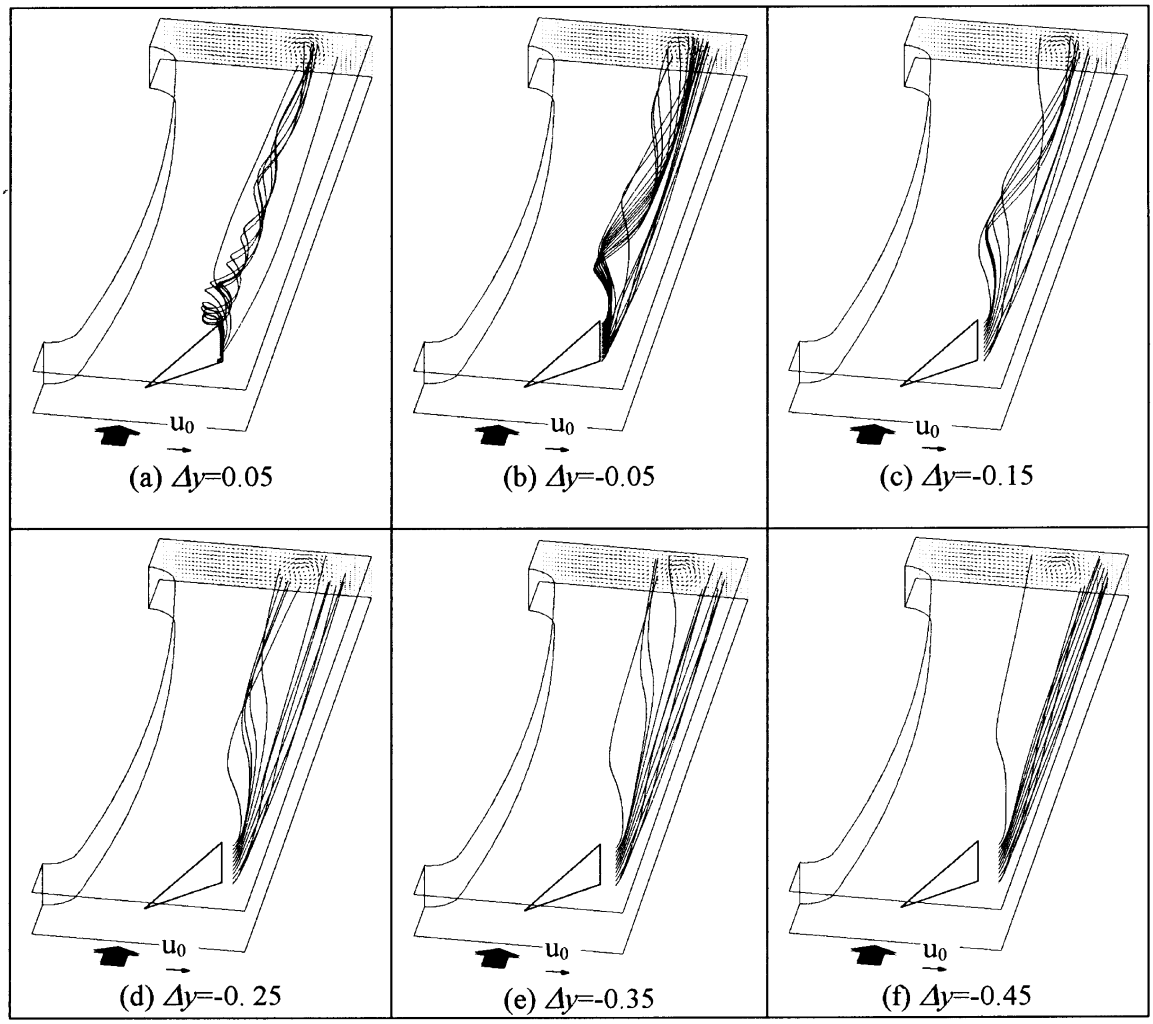

Fig. 7. Streamlines starting from different distances to the trailing edge of the winglet, config. 1, $Re = 300$.

in the vicinity of the winglet (see Fig. 11). The minimum fin temperature is located near the origin of the coordinate ($x = 0$, $y = 0$) as for the FOT without DWP, but with a lower value. Near the origin, the fin temperature of config. 2 ($\beta = 45^\circ$) is lower than that of config. 3 ($\beta = 30^\circ$). This changes near the exit, where the fin temperatures of config. 2 are higher than those of config. 3.

The swirling flow rearranges the temperature distribution in the fluid, as shown in the temperature distributions in eight y–z-planes in Fig. 12. The temperatures in the outer layer of the LV are higher than that in the LV core. In the section of $y \approx 2$ (near the side of the DWP tip), the temperature boundary layers are thinned on the lower fin and thickened on the upper fin, in contrast to that along $y \approx 1$ (near the trailing edge side of the DWP). The distorted temperature boundary layers on the fins break the U-shape distribution of isotherms of an FOT without DWP [10].

Figure 13(a)–(b) shows the local heat fluxes $\dot{q}$ for config. 3 and config. 2, and Fig. 13(c)–(d) the Nusselt numbers on both sides of the fin in config. 2 for $Re = 300$ and $Fi = 500$. In the wake of the winglet, the isolines are formed with three peaks—one higher peak with two lower ones on both sides. The higher peak is a result of the primary vortices, while the lower ones stem from the secondary vortices. $\dot{q}$ is higher for config. 2 than for config. 3, except near the exit, where heat transfer of config. 2 seems weaker than that of config. 3. On both sides of the LVs, fluid flows either towards or away from the fin (the 'Down-wash' and 'Up-wash' flow), which enhances or lowers the heat transfer in the corresponding area. Figure 13(c)–(d) compares the local Nusselt num-

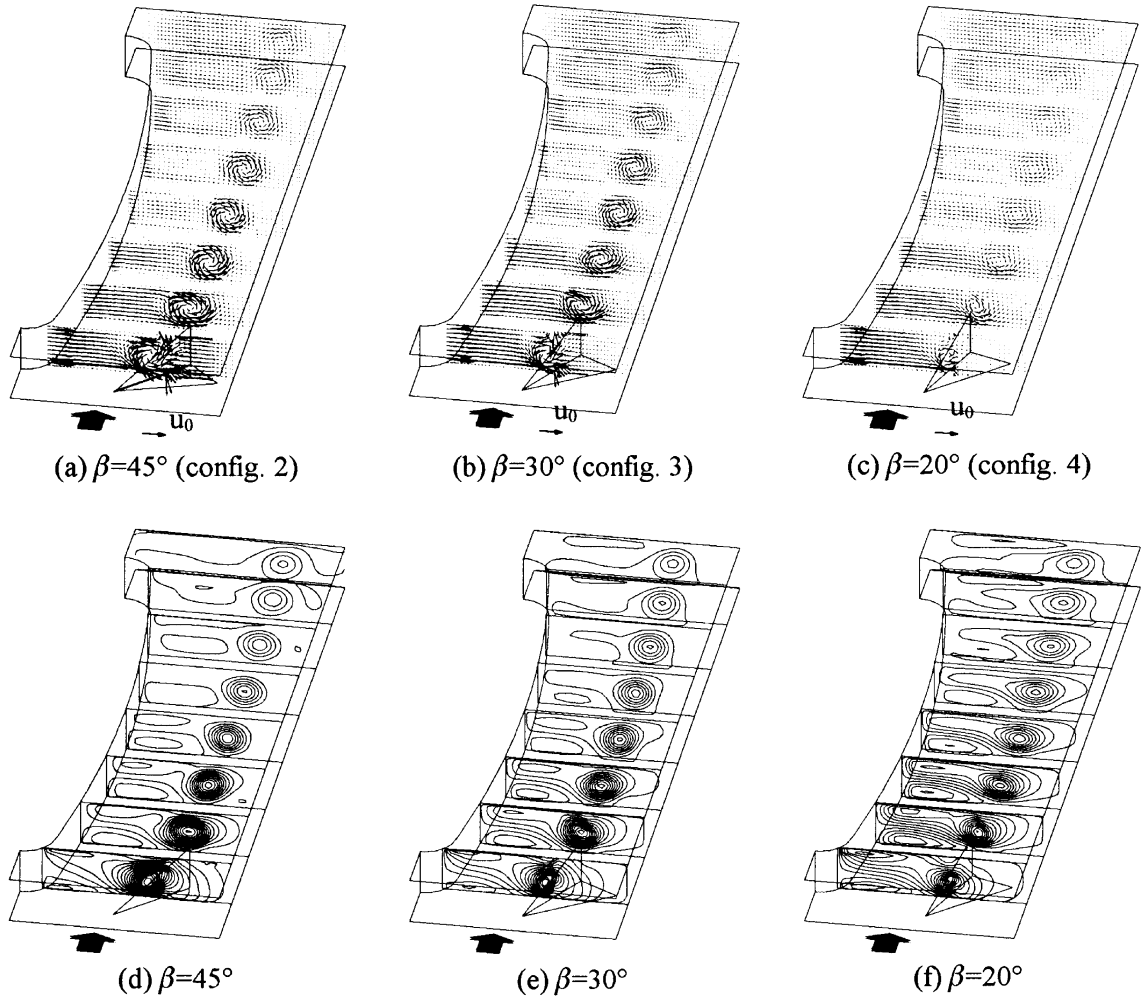

Fig. 8. Velocity vectors and streamlines of the secondary flow generated by DW with three angles of attack in eight y–z-planes of $x = 1.5, 3.5, 5.6, 7.7, 9.7, 11.8, 13.8, 15.4$ respectively.

bers on both sides of the fin. On the fin with winglet (the lower channel wall in this study), fluid flows towards the fin in the tip side of the winglet and away from the fin in the trailing edge side. These lead to higher heat transfer along the tip side and lower heat transfer along the trailing edge side. These are just the opposites to the side without DWP, where higher heat transfer along the trailing edge side and lower heat transfer along the tip side of the winglet appear.

4. Performance comparison

4.1. *Influences of the* x*-position*

Near the entrance, the largest velocity and temperature gradients occur. To study the performance dependence of the winglet on its position in that high gradient region, two configurations with slightly different x-positions of the winglet were investigated (config. 1 and config. 2). The x-coordinate of the winglet tip was 1.46 for config. 1 and 0.63 for config. 2. Figure 14(a) and (b) compares the spanwise averaged pressure distribution and the Nusselt number enhancement (Nu/Nu_0) of config. 1 and config. 2 (Nu_0 refers to the Nusselt number in config. 0). The pressure loss in config. 1 is slightly larger than that in config. 2 because of a larger form drag. The largest difference occurs between $x \approx 1.5$ to 3. Then it decreases gradually in the streamwise direction. Heat transfer enhancement for config. 2 takes place further upstream than that of config. 1. Though Nu/Nu_0 for config. 1 is larger than for config. 2 in the downstream part of the fin, the difference in total heat transfer enhancement is negligible for both configurations due to the com-

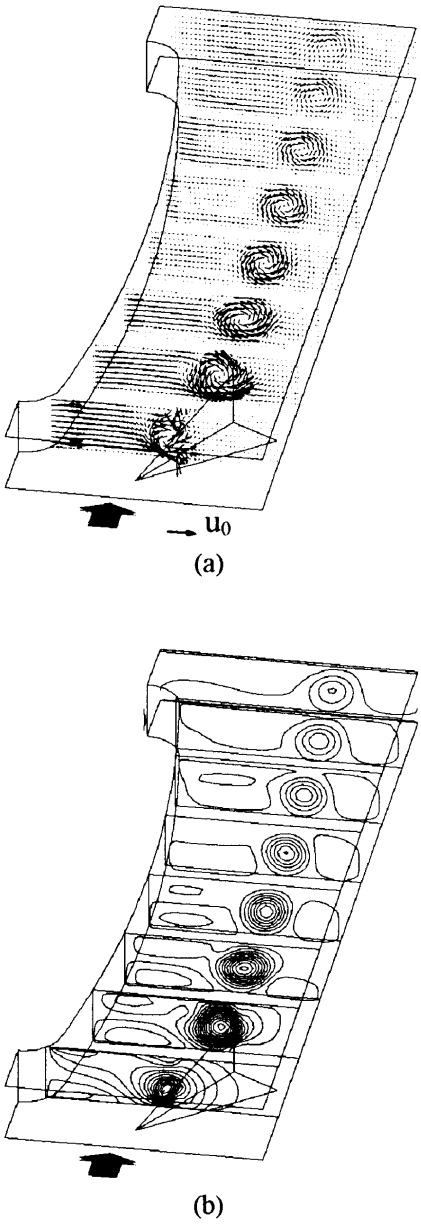

Fig. 9. Vector-plots (a) and streamlines (b) of the secondary flow generated by the delta winglet ($\Lambda = 1.5$, $\beta = 30^\circ$) in different x-sections (location as in Fig. 8) for $Re = 300$.

pensation of the larger Nu_0 near the entrance. In case of $Re = 300$ and $Fi = 500$, the thermohydraulic performance factor $R_P = (j/j_0)/(f/f_0)$ for config. 2 is $R_P = 0.96$, which is slightly superior to that for config. 1 with $R_P = 0.94$.

4.2. Influences of β

In the investigated range of β, both heat transfer and pressure drop increase with increasing β. Figure 15(a) and (b) shows the spanwise averaged pressure distribution and Nusselt number enhancement compared to an FOT without DWP. Comparing the p-distribution of an FOT with and without winglet, two parts of form drag can be distinguished, one from the tube and the other from the winglet. The parallelism of the p-curves in the wake of the winglet indicates that the LVs themselves play little role in the FLP, as deduced by Fiebig [34] from the global drag values of an experimental investigation. The form drag of the winglets are dominant for FLP. Nu/Nu_0 climbs abruptly with the beginning of the leading edge of the winglet and descends abruptly directly behind the winglet. These are the combined effects of the HTE on the fin (the secondary surface [1]) produced by the LVs and the HTE on the winglet surface (the tertiary surface [1]) itself because of the direct contact of the winglet surface with the core flow. The peak value of the Nu-curve for the winglet with $\beta = 45^\circ$ is about the same as that with $\beta = 30^\circ$, which is higher than that with $\beta = 20^\circ$. Generally, Nu/Nu_0 increases with increasing β. Downstream of $x \approx 9$, the curve for $\beta = 45^\circ$ surprisingly crosses that for $\beta = 30^\circ$ and remains under the latter. Comparing the pressure distribution and the Nusselt number enhancement, we notice that the difference in pressure drop between $\beta = 30^\circ$ and $\beta = 20^\circ$ is smaller than that between $\beta = 30^\circ$ and $\beta = 45^\circ$, while the difference in (Nu/Nu_0) is just the opposite of that. The values of R_P for the winglet with $\beta = 45^\circ$, 30° and 20° are 0.96, 1.04 and 1.02 respectively.

4.3. Influences of Λ

HTE and FLP increase with decreasing aspect ratio Λ. Figure 16(a) and (b) compares the pressure distribution and Nu enhancement for $\Lambda = 2$ (config. 3) and $\Lambda = 1.5$ (config. 5). From Fig. 16(b), we see that the peak of the curve for $\Lambda = 1.5$ is apparently higher and wider than that of the curve for $\Lambda = 2$. HTE is higher for $\Lambda = 1.5$, until $x \approx 11$ where the two curves merge. The values of R_P are 1.04 and 1.02 for $\Lambda = 2$ and 1.5 respectively.

5. Concluding remarks

Flow field analysis reveals:

- The form drag of the winglet dominates the FLP, the LVs themselves hardly cause any additional pressure drop.
- The core of the primary LV stems from fluid on the lower part of the leading edge of the winglet.
- The body and the outer layer of the primary LV are

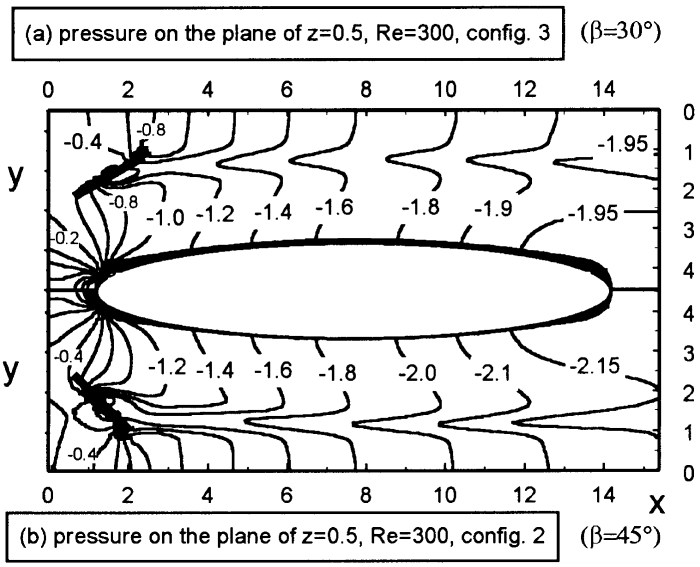

Fig. 10. Comparison of the pressure distribution on the plane of $z = 0.5$ for config. 2 and 3 with $Re = 300$.

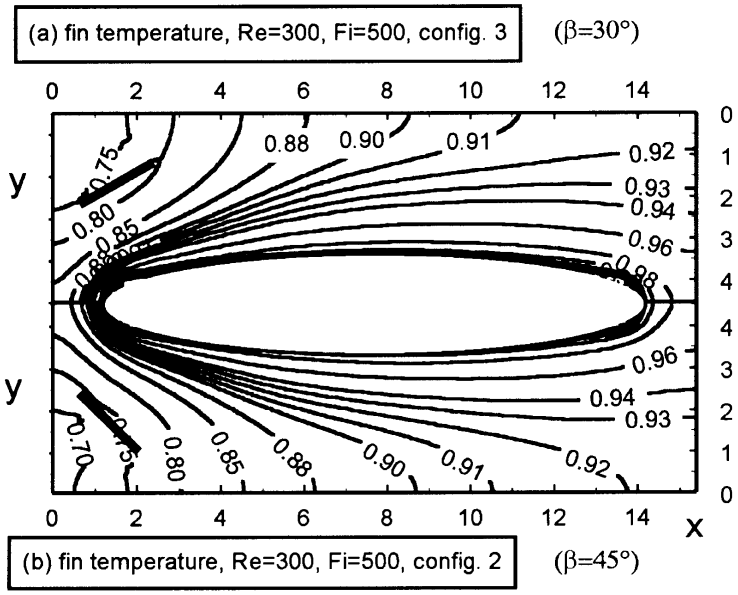

Fig. 11. Fin temperature for two configurations with $Re = 300$, $Fi = 500$.

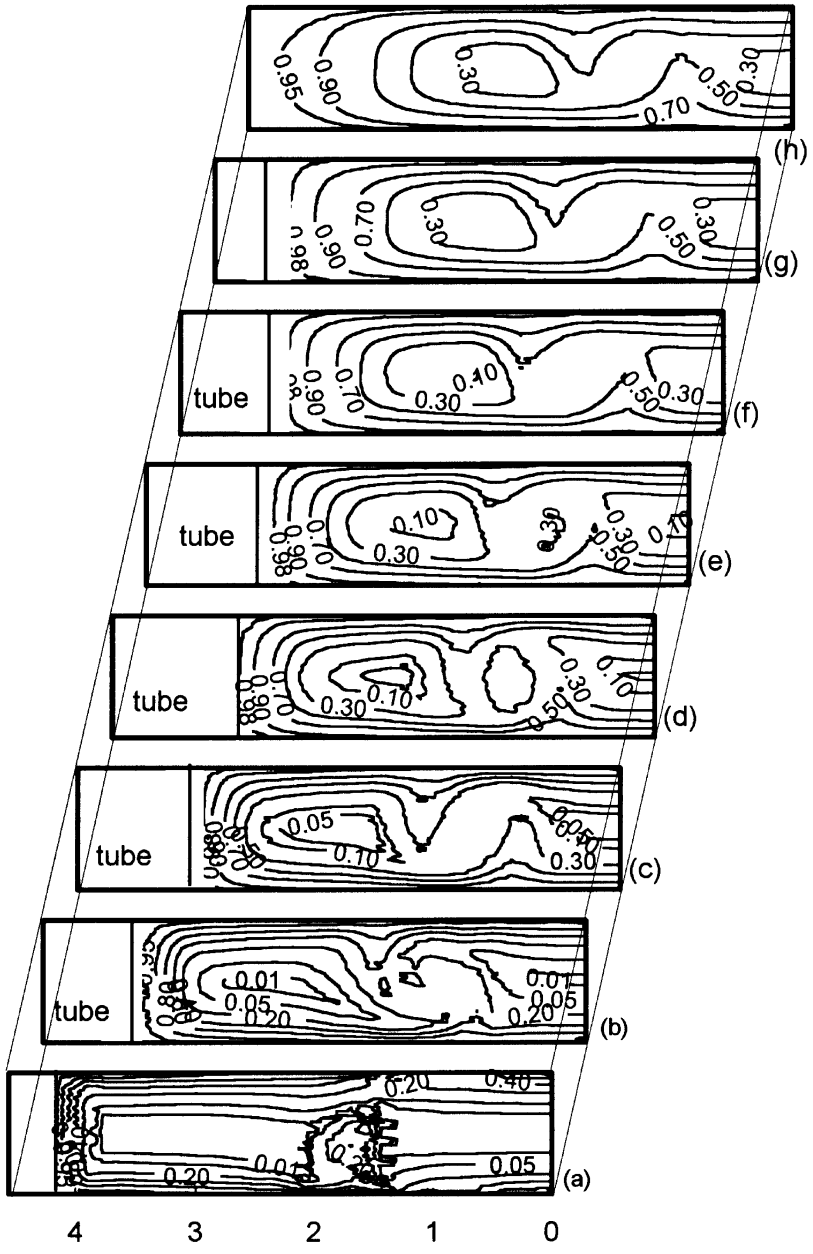

Fig. 12. Isotherms in eight x-sections of an FOT with DWP of $\beta = 45^\circ$ for $Re = 300$, $Fi = 500$. From (a) to (h), $x = 1.5$, 3.5, 5.6, 7.7, 9.7, 11.8, 13.8, and 15.4.

formed by the fluid near the leading edge and near the upper part of the trailing edge of the winglet.

- A corner vortex is formed by fluid from the lower part of the trailing edge and the fluid near the tip of the winglet.
- The y-coordinate of the LV core changes slightly in the streamwise direction due to the flow around the tube.

The LVs swirl the flow and enhance the heat transfer.

Performance comparison of the investigated configurations shows:

- Winglet with $\beta = 30^\circ$ and $\Lambda = 2$ (config. 3) are the best of the investigated configurations.
- A slight change of the DWP position from $x_{PA} = 1.46$ to $x_{PA} = 0.63$ has little change in heat transfer, but reduces the flow loss slightly, so that the ratio of HTE to FLP is slightly higher for the latter position.

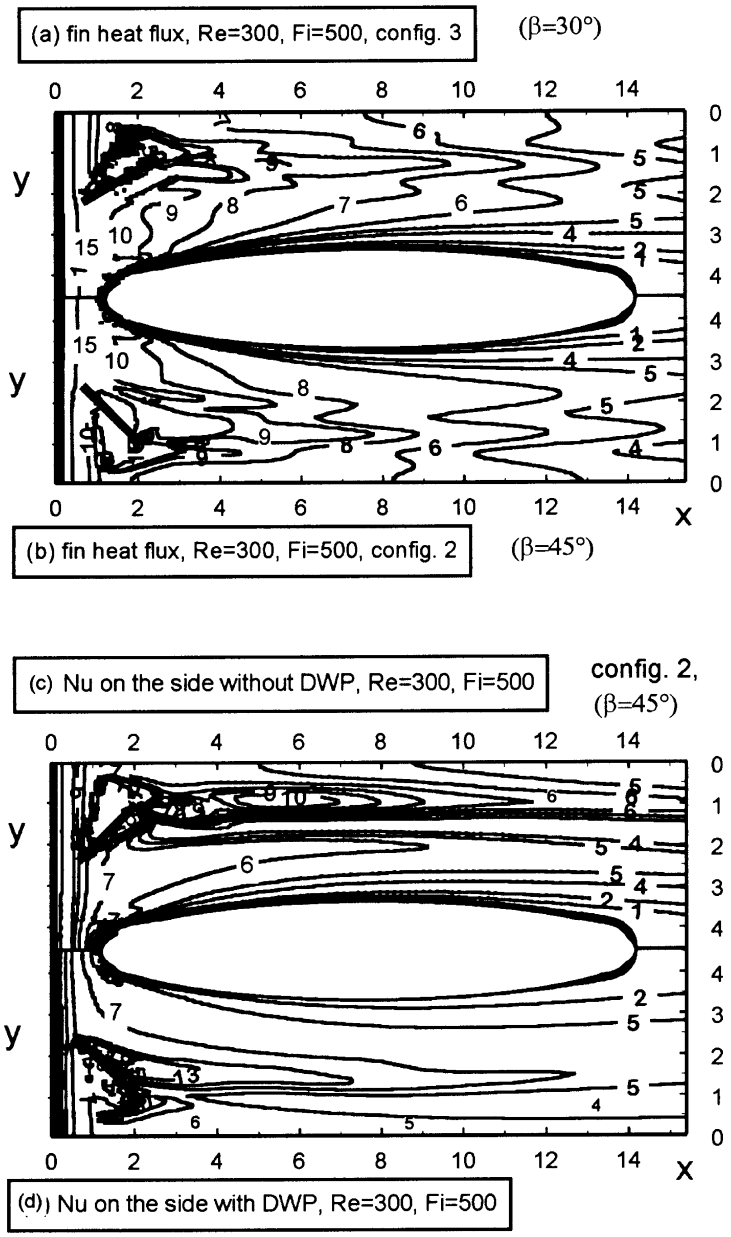

Fig. 13. (a)–(b) Comparison of the fin heat flux in config. 2 and config. 3. (c)–(d) Comparison of the Nusselt number on the side with and without delta winglet in config. 2 ($\beta = 45°$).

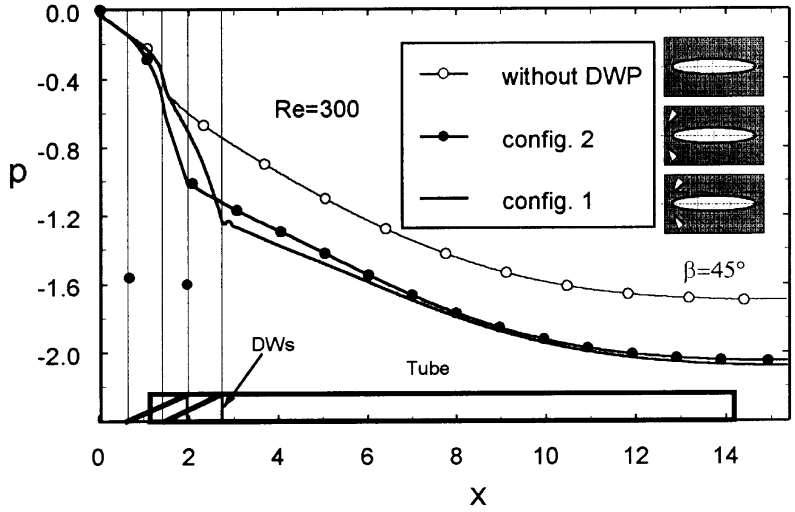

(a) cross-sectional averaged pressure distribution

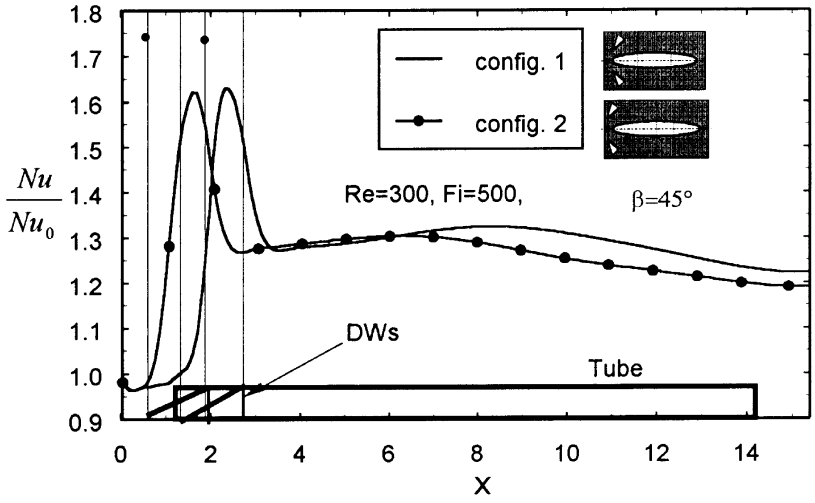

(b) span-averaged *Nu* enhancement

Fig. 14. Comparison of the pressure distribution and heat transfer enhancement of config. 1 and config. 2 with $Re = 300$, $Fi = 500$. Nu_0 is the Nusselt number in an FOT without winglet.

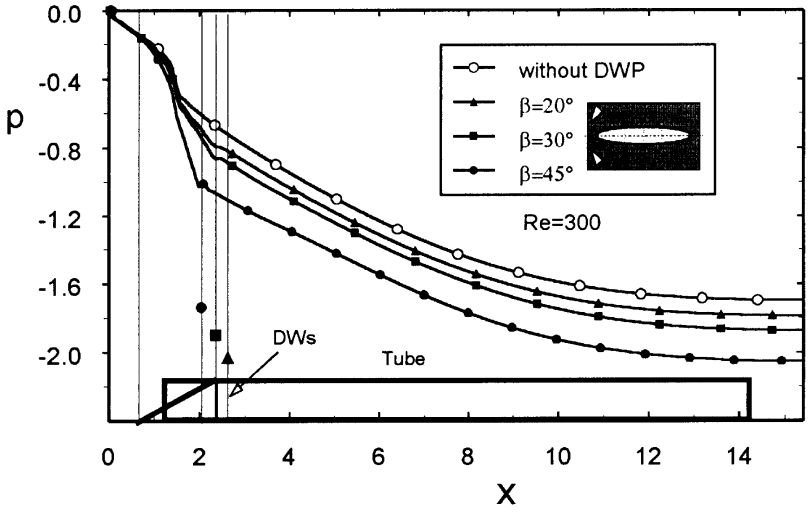

(a) cross-sectional averaged pressure distribution

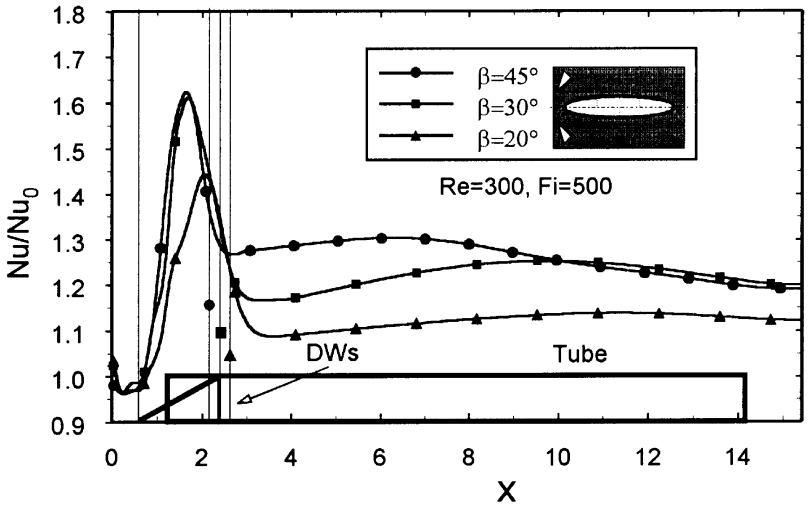

(b) span-averaged *Nu* enhancement

Fig. 15. Comparison of the pressure distribution and heat transfer enhancement of configs. 2, 3, and 4 ($\beta = 45°$, 30°, and 20°) with $Re = 300$, $Fi = 500$. Nu_0 is the Nusselt number in an FOT without winglet.

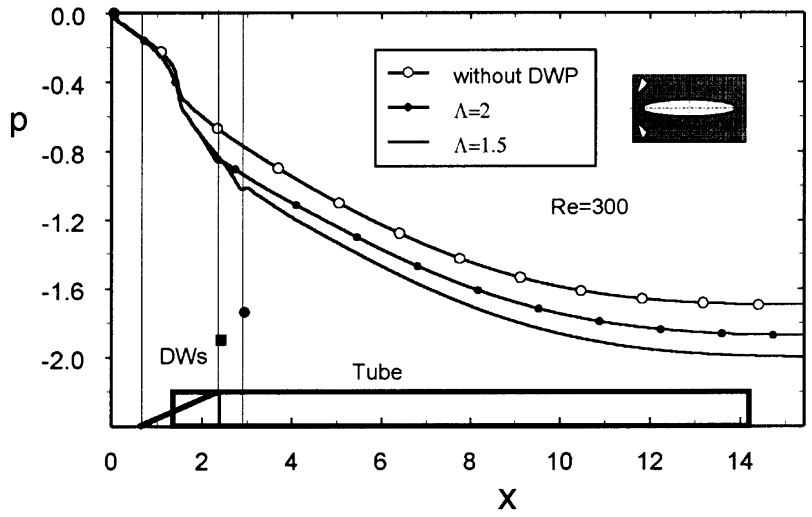

(a) cross-sectional averaged pressure distribution

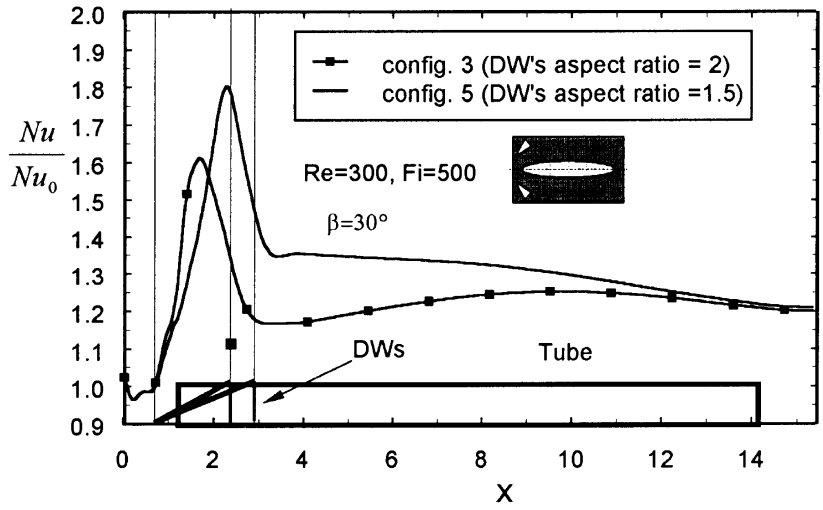

(b) span-averaged *Nu* enhancement

Fig. 16. Comparison of the pressure distribution and heat transfer enhancement of config. 3 and config. 5 with $Re = 300$, $Fi = 500$. Nu_0 is the Nusselt number in an FOT without winglet.

References

[1] Fiebig M. Vortex generators for compact heat exchangers, Int. J. of Enhanced Heat Transfer 1995;2:43–61.

[2] Fiebig M. Embedded vortices in internal flow: heat transfer and pressure loss enhancement. Int. J. of Heat and Fluid Flow 1995;16:376–88.

[3] Fiebig M. Vortices and heat transfer. ZAMM, Z. Angew. Math. Mech. 1997;77:3–18.

[4] Jacobi AM, Shah RK. Heat transfer surface enhancement through the use of longitudinal vortices : a review of recent progress. Exp. Therm. Fl. Sci. 1995;11:295–309.

[5] Torii K, Nishino K, Nakayama K. Mechanism of heat transfer augmentation by longitudinal vortices in a flat plate boundary layer. Proc. 10th IHTC, Brighton, UK, 1994;6:123–8.

[6] Yanagihara JI, Torii K. Heat transfer augmentation by longitudinal vortices rows. Exp. Heat Transfer, Fluid Mechanics and Thermodynamics 1993, 560–7.

[7] Tiggelbeck S. Experimentelle Untersuchungen an Kanalströmungen mit Einzel- und Doppelwirbelerzeuger-Reihen für den Einsatz in kompakten Wärmetauschern. Dissertation, Institut für Thermo- und Fluiddynamik, Ruhr-Universität Bochum, Germany, 1990.

[8] Güntermann T. Dreidimensionale stationäre und selbsterregt-schwingende Strömungs- und Temperaturfelder in Hochleistungswärmeübertragern mit Wirbelerzeugern. Dissertation, Institut für Thermo- und Fluiddynamik, Ruhr-Universität Bochum, Germany, 1992.

[9] Fiebig M, Grosse-Gorgemann A, Chen Y, Mitra NK. Conjugate heat transfer of a finned tube. Part A : Heat transfer behavior and occurrence of heat transfer reversal. Numerical Heat Transfer, Part A 1995;28:133–46.

[10] Chen Y, Fiebig M, and Mitra NK. Conjugate heat transfer of a finned oval tube. Numerical Heat Transfer, Part A 1998 ;33:371–401.

[11] Fiebig M, Chen Y, Grosse-Gorgemann A, Mitra, NK. Conjugate heat transfer of a finned tube. Part B : Heat transfer augmentation and avoidance of heat transfer reversal by LVG. Numerical Heat Transfer, Part A 1995;28:147–55.

[12] Biswas G, Mitra NK, Fiebig M. Heat transfer enhancement in a fin-tube heat exchangers by winglet type vortex generators. Int. J. Heat Mass Transfer 1994;37:283–91.

[13] Sanchez M. Numerische Simulation von einreihigen Lamellen-Rohr-Wärmeübertragern mit Längswirbelerzeugern. Dissertation, Institut für Thermo- und Fluiddynamik, Ruhr-Universität Bochum, Germany, 1991.

[14] Russell CMB, Jones TV, Lee GH. Heat transfer enhancement using vortex generators. Proc. 7th IHTC, München 1982;3:283–8.

[15] Valencia A. Wärmeübergang und Druckverlust in Lamellen-Rohr-Wärmeübertragern mit Längswirbelerzeugern. Dissertation, Institut für Thermo- und Fluiddynamik, Ruhr-Universität Bochum, Germany, 1993.

[16] Kays WM, London AL. Compact Heat Exchangers. 3rd Edition, McGraw-Hill Book Company, New York, 1984.

[17] Hilgenstock, A., A fast method for elliptic generation of 3D grids with full boundary control. In : Sengupta S, et al., editors. Numerical Grid Generation in Computational Fluid Mechanics, Swansea: Pineridge, 1988. pp. 137–46.

[18] Patanker SV. Numerical Heat Transfer and Fluid Flow, Hemisphere Publishing Corporation, 1980.

[19] Khosla PK, Rubin SG. A diagonally dominant second-order accurate implicit scheme. Comp. Fluids 1974;2:207–9.

[20] Van Doormaal JP, Raithby GD. Enhancements of the SIMPLE method for predicting incompressible fluid flows. Numerical Heat Transfer 1984;7:147–63.

[21] Rhie CM, Chow WL. Numerical study of the turbulent flow past an airfoil with trailing edge separation. AIAA J. 1983;21:1525–32.

[22] Stone HL. Iterative solution of implicit approximations of multidimensional partial differential equations. SIAM J. Numer. Anal. 1968;5:530–58.

[23] Peric M. A finite volume method for the prediction of three-dimensional fluid flow in complex ducts. PhD Thesis, University of London, 1985.

[24] Kost A. Strömungsstruktur und Drehmomentübertragung in hydrodynamischen Kupplung. Dissertation, Institut für Thermo- und Fluiddynamik, Ruhr-Universität Bochum, Germany, 1993.

[25] Chen Y. Leistungssteigerung von Wärmeübertragern mit berippten Ovalrohren durch Längswirbelerzeuger—Numerische Simulation von Strömung und konjugiertem Wärmeübergang. Shaker Verlag, Aachen, Germany, 1998.

[26] Große-Gorgemann A. Numerische Untrsuchung der laminaren oszillierenden Strömung und des Wärmeüberganges in Kanälen mit rippenförmigen Einbauten. Dissertation, Institut für Thermo- und Fluiddynamik, Ruhr-Universität Bochum, Germany, 1995.

[27] Bai L. Numerische Untersuchung von turbulenten Strömungen in hydrodynamischen Kupplungen. Dissertation, Institut für Thermo- und Fluiddynamik, Ruhr-Universität Bochum, Germany, 1994.

[28] Roache PJ. A method for uniform reporting of grid refinement studies. In : Quantification of Uncertainty in Computational Fluid Dynamics, ASME FED-Vol. 158, 1993, pp. 109–20.

[29] Shah RK, Bhatti MS. Laminar convective heat transfer. In Kakaç S, Shah RK, Aung W. editors. Handbook of Single-Phase Convective Heat Transfer, John Wiley & Sons, 1987.

[30] Hagedorn M. Untersuchung des Wärmeüberganges und des Strömungsverlustes an Lamellen-Rohr-Wärmeübertragermodulen unter Berücksichtigung der Wärmeleitung in den Lamellen. Diplomarbeit Nr. 95-07, Institut für Thermo- und Fluiddynamik, Ruhr-Universität Bochum, Germany, 1995.

[31] Neumann H. Private communication. Institut für Thermo- und Fluiddynamik, Ruhr-Universität Bochum, Germany, 1997.

[32] Hagedorn M. Private communication. Institut für Thermo- und Fluiddynamik, Ruhr-Universität Bochum, Germany, 1997.

[33] Biswas G, Torii K, Fujii D, Nishino K. Numerical and experimental determination of flow structure and heat transfer effects of longitudinal vortices in a channel flow. Int. J. Heat Mass Transfer 1996;39:3441–51.

[34] Fiebig M, Kalweit P, Mitra NK. Wing Type Vortex Generators for Heat Transfer Enhancement. Proc. 8th IHTC, Vol. 6, 1986, pp. 2909–13.